ACS OMEGA

Article

Cite This: ACS Omega 2018, 3, 3235−3247

Liquid Crystalline Nanostructures as PEGylated Reservoirs of Omega-3 Polyunsaturated Fatty Acids: Structural Insights toward Delivery Formulations against Neurodegenerative Disorders

Angelina Angelova,*[,†] Markus Drechsler,[‡] Vasil M. Garamus,[§] and Borislav Angelov[∥]

[†]Institut Galien Paris-Sud, LabEx LERMIT, CNRS UMR 8612, Univ. Paris-Sud, Université Paris-Saclay, F-92290 Châtenay-Malabry Cedex, France

[‡]Key Lab "Electron and Optical Microscopy", Bavarian Polymer Institute (BPI), University of Bayreuth, D-95440 Bayreuth, Germany

[§]Helmholtz-Zentrum Geesthacht: Centre for Materials and Coastal Research, D-21502 Geesthacht, Germany

[∥]Institute of Physics, ELI Beamlines, Academy of Sciences of the Czech Republic, Na Slovance 2, CZ-18221 Prague, Czech Republic

ABSTRACT: Omega-3 polyunsaturated fatty acids (ω-3 PUFAs) are bioactive lipids with considerable impact in medicine and nutrition. These compounds exert structuring effects on the cellular membrane organization, regulate the gene expression, and modulate various signaling cascades and metabolic processes. The purpose of the present work is to demonstrate the structural features of ω-3 PUFA-containing three-dimensional supramolecular lipid assemblies suitable for pharmaceutical applications that require soft porous carriers. We investigate the liquid crystalline structures formed upon mixing of eicosapentaenoic acid (EPA, 20:5) with the lyotropic nonlamellar lipid monoolein and the formation of multicompartment assemblies. Starting with the monoolein-based lipid cubic phase, double membrane vesicles, cubosome precursors, sponge-type particles (spongosomes), mixed intermediate nonlamellar structures, and multicompartment assemblies are obtained through self-assembly at different amphiphilic compositions. The dispersions containing spongosomes as well as nanocarriers with oil and vesicular compartments are stabilized by PEGylation of the lipid/water interfaces using a phospholipid with a poly(ethylene glycol) chain. The microstructures of the bulk mixtures were examined by cross-polarized light optical microscopy. The dispersed liquid crystalline structures and intermediate states were studied by small-angle X-ray scattering, cryogenic transmission electron microscopy, and quasielastic light scattering techniques. They established that PUFA influences the phase type and the sizes of the aqueous compartments of the liquid crystalline carriers. The resulting multicompartment systems and stealth nanosponges may serve as mesoporous reservoirs for coencapsulation of ω-3 PUFA (e.g., EPA) with water-insoluble drugs and hydrophilic macromolecules toward development of combination treatment strategies of neurodegenerative and other diseases.

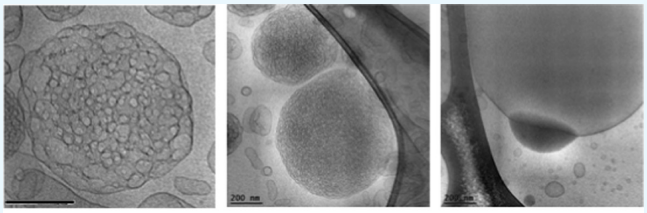

Liquid crystalline lipid carriers containing EPA

INTRODUCTION

The necessity of improved safety of the currently developed drug delivery systems, aiming at reduced side effects, strongly stimulates the research on naturally occurring products, biomimetic and bio-inspired materials, and components.[1−12] Lipid-based nanostructured dispersions are well recognized as gentle and biocompatible drug delivery systems.[13−20] Cubosomes, hexosomes, spongosomes, or vesicular lipid assemblies are fabricated depending on the amphiphilic compositions and the employed dispersing agents.[21−57] Among the nanostructured carriers, the liquid crystalline lipid assemblies have shown considerable potential in protecting instable encapsulated molecules from degradation and enhancing their bioavailability and diffusion through the biological barriers.[2,15,24,36,43,47−50]

The health benefits of omega-3 polyunsaturated fatty acids (ω-3 PUFAs) and their influence on the membrane structure and functions have attracted significant interest.[58−81] The aim has been a better comprehension of the membrane fusion mechanism, the induction of higher curvature regions or transient tubular intermediates in the subcellular compartments, the possible non-bilayer phase formation, the effects on the protein activity in the plasma membranes and the synaptosome, the activation of signaling cascades, enzymatic regulation, gene expression, stress responses, and the prevention of inflammation reactions.[58,59,79−96] The current interest in the ω-3 PUFAs properties is motivated by the fact that this class of bioactive lipids is implicated in a number of diseases related to neurodegeneration, ageing, inflammation, depression, vision, anterior ischemic optic neuropathy, atherosclerosis, coronary heart disease, etc.[82−96] The neuroprotective effects of the ω-3 PUFA derivatives are of particular importance for upcoming pharmaceutical applications in which

Received: December 5, 2017
Accepted: March 6, 2018
Published: March 16, 2018

DOI: 10.1021/acsomega.7b01935
ACS Omega 2018, 3, 3235−3247

these lipids may exert protection against neurotoxin-induced cell apoptosis.

The long-chain ω-3 PUFAs like *cis*-5,8,11,14,17-eicosapentaenoic acid (EPA) (20:5) and *cis*-4,7,10,13,16,19-docosahexaenoic acid (22:6) are amphiphiles with a nonlamellar propensity, which are considered as membrane structuring lipids.[62,76] They may be expected to generate synthetic liquid crystalline structures with new properties when self-assembled with "helper" lipids (Scheme 1). The structural effects of ω-3 PUFAs have been scarcely investigated in three-dimensional (3D) supramolecular assemblies as compared to their influence on the membrane fluidity and ion permeability.[53,63,64,76] So far, PUFAs have been demonstrated to reduce the membrane bilayer thickness, increase the membrane fluidity, and boost the membrane permeability in connection with possible domain formation or induction of negative curvature strain.[61,65−72,77,81]

Scheme 1. Molecular Structures of Eicosapentaenoic Acid (EPA) and Monoolein (MO)

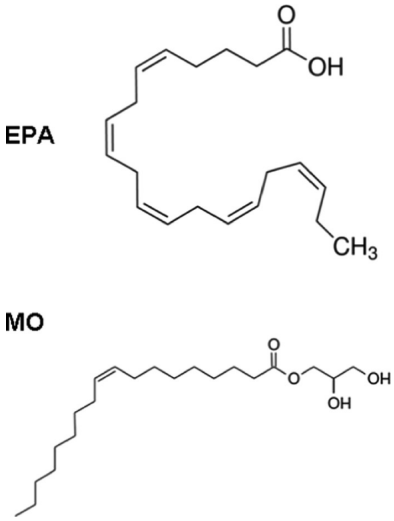

It should be noted that the ω-3 polyunsaturated fatty acids are poorly water-soluble compounds of low stability upon administration. Delivery of PUFAs and fish-oil-based formulations has been done using oil-in-water emulsions.[97−102] Oxidative stability of the lipid dispersions has been achieved by coencapsulation of PUFAs with natural antioxidants.[50] The recently developed internally self-assembled nanostructured carriers (ISAsomes)[32] offer new opportunities for encapsulation and delivery of PUFAs as bioactive lipid ingredients. Such carrier particles (cubosomes, hexosomes, or spongosomes) do not rapidly break upon contact with biological fluids after administration and may provide sustained release.[3,6,24,43,44,49] Moreover, they can be sterically stabilized by hydrophilic shells to avoid eventual aggregation in the milieu.[3,10,14,29,47,48]

The purpose of the present work is to reveal the multiscale structural organization of EPA-encapsulating carrier lipid systems for potential uses in neuroregenerative therapies. The structural modifications triggered by the incorporation of EPA (as a representative ω-3 PUFA) in monoolein (MO) lyotropic liquid crystalline assemblies are investigated by small-angle X-ray scattering (SAXS) and cryogenic transmission electron microscopy (cryo-TEM). The hydrated bulk mixtures are characterized by cross-polarized light optical microscopy (POM). The quasielastic light scattering (QELS) technique is also applied to get insights into the mechanism of formation of stable nanodispersions involving the bioactive lipid EPA.

RESULTS AND DISCUSSION

We present morphological and structural results characterizing the properties of hydrated bulk and nanodispersed lipid mixtures of eicosapentaenoic acid (EPA) and monoolein (MO) at varying molar contents. The spontaneously self-assembled mesophase structures are governed by the intermolecular interactions and the curvature preferences of the lipid components in the mixtures, i.e., by their mean critical packing parameters (CPP).[8] MO is a lyotropic lipid forming bicontinuous cubic structures in excess aqueous medium.[22,30] EPA, as a long-chain ω-3 PUFA compound with five double bonds (Scheme 1), has a nonlamellar propensity in membranes.[61] However, it has not been reported to form lyotropic nonlamellar liquid crystalline structures as a single-component amphiphile. By mixing of EPA with the lyotropic lipid MO, we accomplished tuning of the average critical packing parameter of the binary mixtures, which provoked the induction of intermediate liquid crystalline states between 3D cubic and 3D sponge-like lipid membrane organizations.

Liquid Crystalline Phase Transitions of Bulk Mixtures Established by POM. The microstructures of bulk mixtures of EPA and MO and the composition-induced lyotropic phase changes were studied by cross-polarized light optical microscopy (POM). The purpose was to inspect the occurrence of an eventual macrodomain phase separation, which may be a problem for the preparation of dispersed nanocarriers. Figure 1 presents POM images of a hydrated self-assembled MO/EPA mixture (90:10 mol/mol) in the absence and in presence of the PEGylated phospholipid (1,2-dioleoyl-*sn*-glycerol-3-phosphoethanolamide-*N*-[methoxy(poly(ethylene glycol))-2000]) (DOPE-PEG_{2000}). At this low molar content of EPA, the obtained thin liquid crystalline layer appeared as an optically isotropic viscous phase typical for a MO cubic phase assembly. The discontinuity of the spread film resulted from the physical agitation and deposition of the viscous sample (Figure 1a−c).

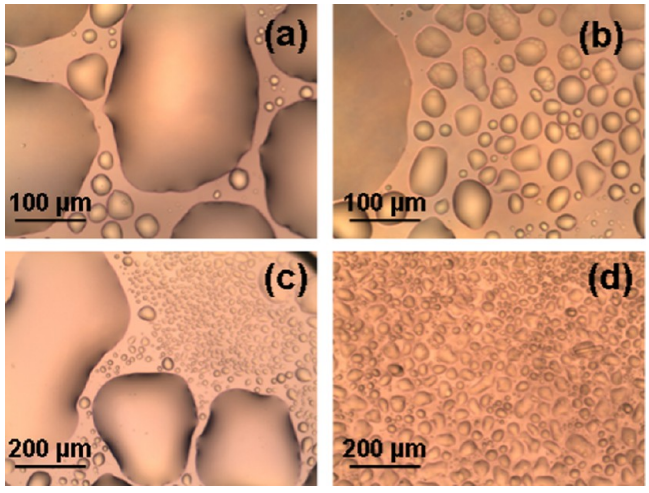

Figure 1. Cross-polarized light optical microscopy (POM) images of a self-assembled mixture of eicosapentaenoic acid and monoolein (MO/EPA ratio 90:10 mol/mol) in the absence (a−c) and in presence (d) of a PEGylated phospholipid (2 mol % DOPE-PEG_{2000}). The hydration level of the bulk sample corresponds to a lipid/water ratio 40:60 (w/w).

DOI: 10.1021/acsomega.7b01935
ACS Omega 2018, 3, 3235−3247

Fragmentation of the bulk bicontinuous cubic phase into smaller entities was observed also by POM upon addition of the PEGylated dispersing agent (2 mol % DOPE-PEG_{2000}) (Figure 1d). The structural dimensions of the cubic unit cells formed in the presence and in the absence of the PEGylated lipid were determined in the small-angle X-ray scattering (SAXS) investigation (see the results presented in Figure 4 below).

Figure 2 shows the POM micrographs of anisotropic liquid crystalline patterns obtained at increasing EPA content in the

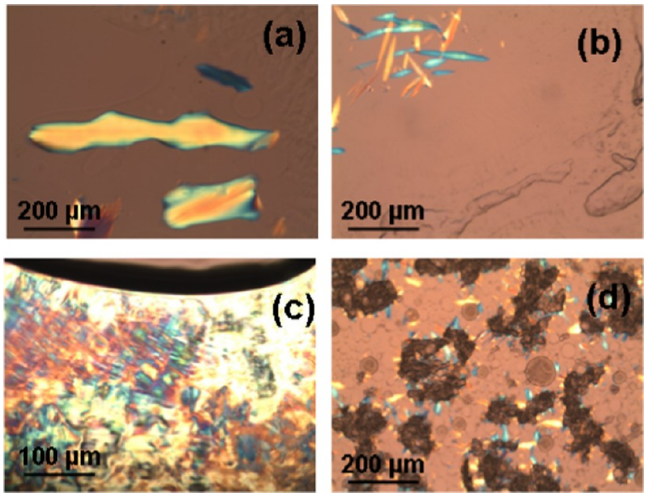

Figure 2. POM micrographs of bulk hydrated MO/EPA mixtures self-assembled at EPA contents, which yield anisotropic bulk liquid crystalline organizations: (a) MO/EPA ratio 85:15 (mol/mol), (b, c) 80:20 (mol/mol), and (d) 70:30 (mol/mol). The lipid/water ratio is 40:60 (w/w).

hydrated bulk MO/EPA mixtures (40 wt % lipid phase; 60 wt % aqueous phase). The inclusion of EPA (from 15 to 50 mol % with regard to MO) led to the nucleation of microdomains corresponding to a structural phase transition from an isotropic bicontinuous cubic to a mixed type of liquid crystalline organization combining both nonlamellar and lamellar structures. The observed birefringence patterns reveal the anisotropic distribution of the lipid membrane curvature, which may reflect the deficiency of embedded EPA with regard to the MO fraction. On the microscopic scale, the examination under cross polarizers did not establish large domains of fan-shaped textures typical for a single inverted hexagonal phase. The texture shown in Figure 2c suggests the presence of a small portion of a lamellar phase. Therefore, the anisotropy of the liquid crystalline supramolecular organization reflects the coexistence of cubic domains (seen as dark areas) and other intermediate structures (birefringence patterns), which grow by nucleation from the isotropic cubic phase (Figure 2). Macroscopic phase separation between the EPA and MO materials was not observed, which demonstrated the capacity of the hydrated nanochanneled structures of MO for solubilization of the ω-3 PUFA component.

At EPA content above 50 mol %, the microtexture of the bulk MO/EPA mixtures adopted an emulsion-type morphology (Figure 3). The large cubic phase domains of irregular boundaries diminished (Figure 3a), whereas the volume occupied by spherical dropletlike textures increased with the increase of the EPA molar fraction (Figure 3b–d). Birefringence patterns were not observed at MO/EPA lipid

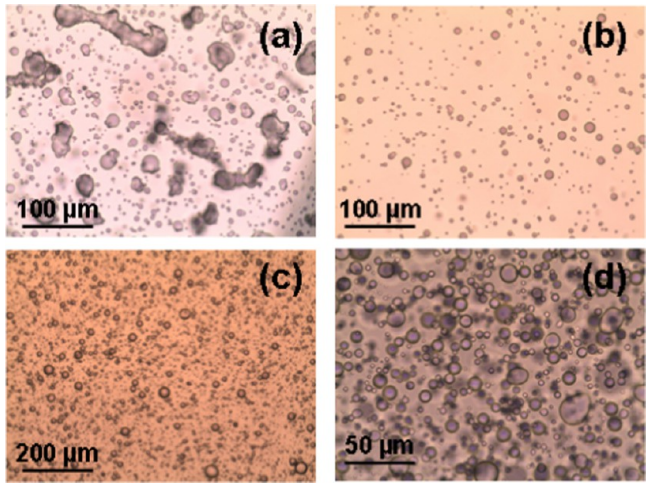

Figure 3. POM micrographs of bulk hydrated MO/EPA mixtures obtained at lipid ratios (a) MO/EPA 50:50 (mol/mol), (b) 30:70 (mol/mol), (c) 20:80 (mol/mol), and (d) 10:90 (mol/mol). The images are recorded at different magnifications using objectives 10× (image size: 880 × 660 μm^2) (c), 20× (image size: 440 × 330 μm^2) (b, c), and 40× (image size: 220 × 165 μm^2) (d). The lipid/water ratio is 40:60 (w/w) in all bulk phase samples.

ratios 30:70 mol/mol (Figure 3b), 20:80 mol/mol (Figure 3c), and 10:90 mol/mol (Figure 3d). This suggested that the binary lipid mixtures undergo a transition from an anisotropic nonlamellar organization to an isotropic phase, which lacks a long-range order. The presence of correlations between the lipid bilayers was examined by SAXS in self-assembled systems dispersed in an excess aqueous phase (see the results in Figure 5 below).

Liquid Crystalline Structural Organization Determined by Small-Angle X-ray Scattering. Hydrated monoolein forms a well-organized bicontinuous cubic phase in excess of aqueous buffer phase, giving a well-resolved diffraction pattern. The effect of the additive, DOPE-PEG_{2000}, on the structure of the MO/water cubic phase is demonstrated by the SAXS results in Figure 4. For the pure MO/water system, the indexing of the detected Bragg peaks identified a

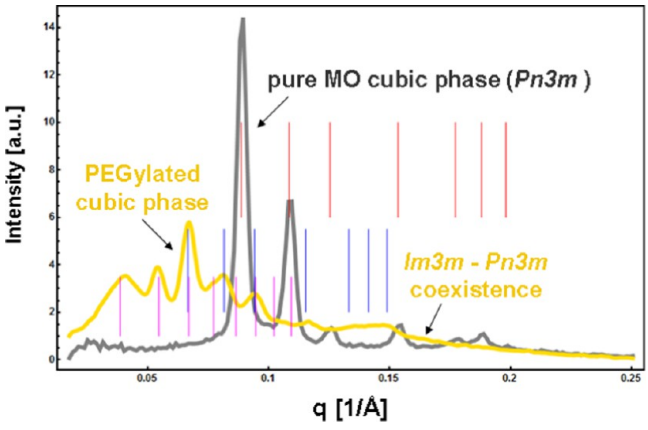

Figure 4. Small-angle X-ray scattering (SAXS) patterns of a bulk phase monoolein/water cubic phase and effect of the addition of a PEGylated lipid on the self-assembled MO/DOPE-PEG_{2000} structure (40 wt % lipid phase/60 wt % aqueous phase). The sets of Bragg peaks are indexed for a *Pn3m* cubic phase (red bars) and for *Im3m*/*Pn3m* cubic phase coexistence (pink and blue bars).

DOI: 10.1021/acsomega.7b01935
ACS Omega 2018, 3, 3235−3247

bicontinuous double diamond cubic phase of the space group *Pn*3*m* and a cubic lattice spacing a = 10.4 nm. The inclusion of the PEGylated lipid induced a cubic-phase coexistence involving primitive *Im*3*m* and double diamond *Pn*3*m* cubic phase domains. The sequences of resolved Bragg peaks determined the following cubic cell dimensions at room temperature: $a(Pn3m)$ = 13.3 nm (with a first Bragg peak positioned at q = 0.067 Å^{-1}) and $a(Im3m)$ = 23.0 nm (with a first Bragg peak positioned at q = 0.039 Å^{-1}). These results demonstrated the increase of the cubic lattice dimension upon addition of the DOPE-PEG$_{2000}$ amphiphile.

The investigated self-assembled mixtures of EPA and MO were functionalized by the PEGylated phospholipid DOPE-PEG$_{2000}$ (at a constant percentage of 2 mol %) toward the fabrication of sterically stabilized nanocarriers upon dispersion by sonication in excess aqueous buffer phase. The structural organizations of the nanoparticulate dispersions obtained at varying MO/EPA ratios were examined by synchrotron radiation SAXS. The dispersions containing low molar fractions of EPA were filtered (using a 0.2 μm pore-sized microporous filter membrane) toward the preparation of sterile-quality nanocarriers necessary for pharmaceutical applications. It can be supposed that lipid material might be lost during the filtration of the nanoparticulate dispersions. For this reason, we report the effect of the filtering on the obtained SAXS patterns.

Figure 5A presents the SAXS results as a function of the amphiphilic composition. The SAXS patterns in Figure 5A (plots 1−4) appear to be representative for liquid crystalline dispersions containing objects of nanoscale sizes, for which the eventual inner periodic organization could not produce strong diffraction peaks. Such objects are visualized by cryo-TEM microscopy in Figures 7 and 8 below.

The SAXS curves of the filtered MO/DOPE-PEG$_{2000}$ and MO/EPA/DOPE-PEG$_{2000}$ dispersions (Figure 5A, plots 1−4) reflect the bilayer membrane organization of the nanoparticles governing their small-angle scattering through the form factor. Bragg peaks of an inner cubic structure are lacking similar to the case of the precursors of MO-based cubosome particles dispersed by polysorbate 80 as a surfactant.[103]

The SAXS patterns acquired at increasing EPA molar fractions indicated the formation of particles of nonlamellar inner organization (Figure 5A, plots 5−7). The inclusion of EPA favored a more dense internal structure of the PEGylated nanocarriers. The nonfiltered lipid membranous assemblies yielded Bragg diffraction peaks at an MO/EPA molar ratio 50:50 (Figure 5A (plot 5) and Figure 5B). Toward the interpretation of the obtained mesostructures, the SAXS pattern was fitted via a superposition of Bragg peaks of several liquid crystalline phases. The performed Bragg peaks indexing for coexisting lamellar, onion bilayer, and inverted bicontinuous cubic structures is demonstrated by the bars of different colors in Figure 5B. The intensities of the Bragg peaks for the lamellar structure are relatively weak and they are positioned at q_1 = 00705 Å^{-1}, q_2 = 0.141 Å^{-1}, q_3 = 0.2115 Å^{-1}, and q_4 = 0.282 Å^{-1}, respectively. The corresponding repeat lamellar distance of the PEGylated multibilayer lipid membranes is d = 8.9 nm. A minor fraction of lipid bilayers arranged in onionlike structures is also present. The Bragg peak at q_1 = 0.134 Å^{-1} determined a repeat spacing L = 4.7 nm. Such onionlike structures are observed in the cryo-TEM micrographs in Figure 11.

The strongest peak of an inverted cubic membrane structure is positioned at q_1 = 0.114 Å^{-1} (Figure 5B) and belongs to a sequence of eight reflections defining the presence of a double

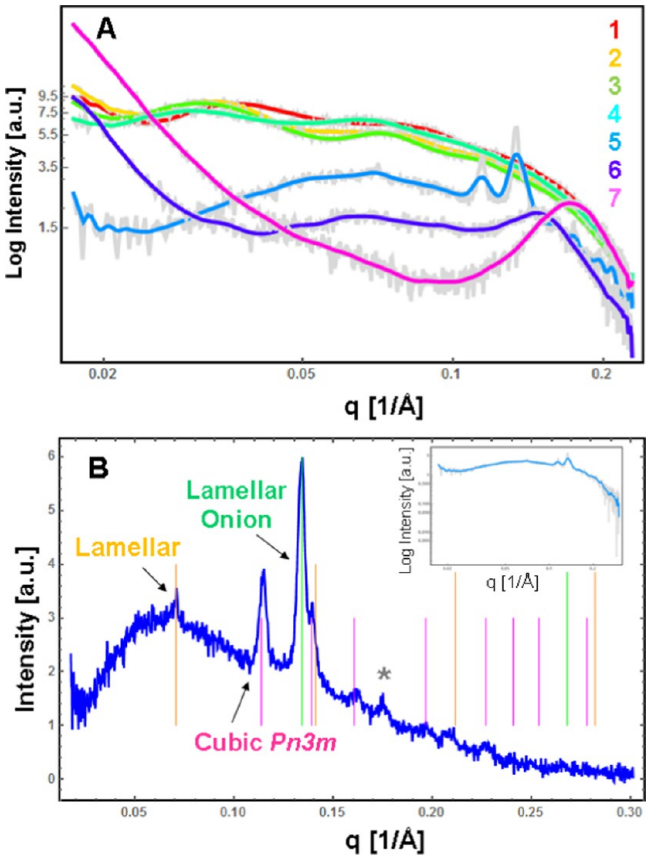

Figure 5. Small-angle X-ray scattering (SAXS) patterns of highly diluted (5 wt % lipid/95 wt % water) dispersions of PEGylated eicosapentaenoic acid/monoolein assemblies MO/EPA/DOPE-PEG$_{2000}$. (A) The MO/EPA ratio varies in the sequence 1:0 mol/mol (plot 1), 85:15 mol/mol (plot 2), 80:20 mol/mol (plot 3), 70:30 mol/mol (plot 4), 50:50 mol/mol (plot 5), 40:60 mol/mol (plot 6), and 30:70 mol/mol (plot 7) at a constant percentage of DOPE-PEG$_{2000}$ (2 mol %) with regard to MO. Aqueous phase: 1 × 10^{-2} M phosphate buffer containing butylated hydroxytoluene (BHT). The samples corresponding to the SAXS plots (5−7) are not sterile-filtered. (B) Indexing of the Bragg peaks recorded at an MO/EPA ratio of 50:50 mol/mol. The inset shows the fitted original SAXS plot (5) from panel (A).

diamond inner cubic organization of the *Pn*3*m* space group. The obtained lattice dimension $a(Pn3m)$ = 7.8 nm revealed the weak hydration of the cubic unit cell at increasing EPA content in the MO/EPA mixtures. The same conclusion was derived from the cryo-TEM results presented below. The weak reflection observed at q_1 = 0.176 Å^{-1} in Figure 5B could not be assigned to a Bragg reflection of a well-ordered lattice. It might correspond to fragments (with internal symmetry) of previously existing three-dimensional structures. One can suppose the formation of different structures or their fragments due to "dissolution" of the cubic phases.

At higher EPA molar fractions (MO/EPA molar ratios 40:60 and 30:70 mol/mol), the strong cubic and lamellar peaks merged into a single broad peak centered at $q \sim 0.15$ Å^{-1} (Figure 5A, plot 6) and at $q \sim 0.18$ Å^{-1} (Figure 5A, plot 7). These broad peaks are interpreted as arising from the fluctuation of the lipid bilayers within the 3D membrane assemblies. The correlation distances of the lipid bilayer membranes are determined to be L = 4.2 nm (plot 6; 60 mol % EPA) and L = 3.5 nm (plot 7; 70 mol % EPA).

DOI: 10.1021/acsomega.7b01935
ACS Omega 2018, 3, 3235−3247

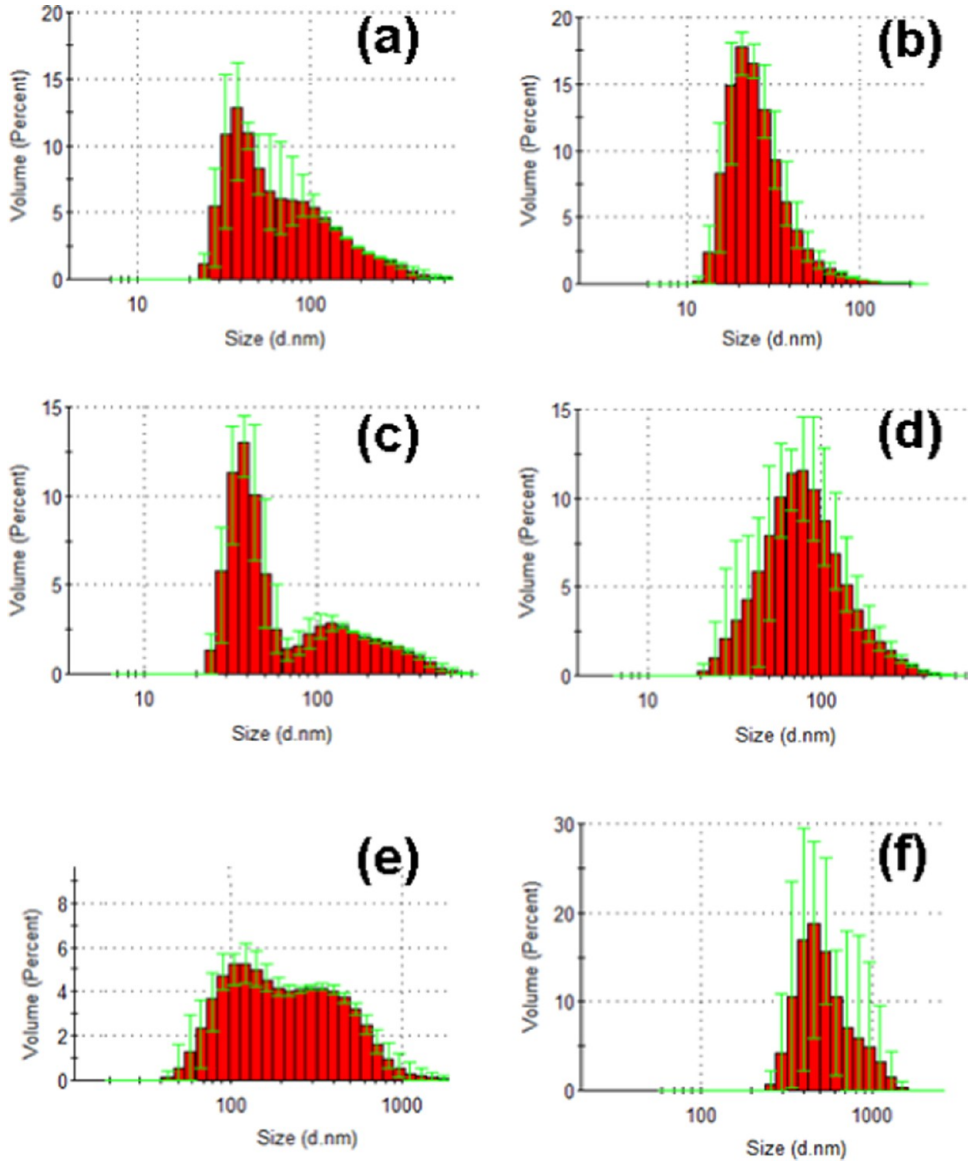

Figure 6. Hydrodynamic nanoparticle size determination by quasielastic light scattering. The MO/EPA molar ratios in the MO/EPA/DOPE-PEG_{2000} dispersions are 1:0 mol/mol (a), 85:15 mol/mol (b), 50:50 mol/mol (c), 70:30 mol/mol (d), 40:60 mol/mol (e), and 30:70 mol/mol (f). The bimodal distributions represent the fractions of small-size and large-size particles coexisting in the sample volumes. Aqueous phase: 1×10^{-2} M phosphate buffer containing BHT.

Evidently, the increase of the EPA content leads to dehydration of the inner structure of the nanocarriers. Taking into account the cryo-TEM results shown in Figures 12 and 13, it can be deduced that the sterically stabilized MO/EPA mixtures may form sponge-type membranous assemblies with tunable dimensions of the aqueous channel compartments depending on the PUFA content. It can be suggested that the EPA-induced membrane curvature change triggers a liquid crystalline phase transition to a randomlike, fluctuating lipid membrane organization, which is consistent with the formation of sponge-type nanocarriers (Figures 12 and 13).

The quasielastic light scattering (QELS) measurements with MO/EPA dispersions stabilized by DOPE-PEG_{2000} indicated the coexistence of nanoparticle populations in some of the recorded size distribution diagrams (Figure 6). The histogram graphs in Figure 6a,c identified a population of small particles, with a mean hydrodynamic diameter centered at $d_h \sim 40$ nm and a second population with a mean diameter centered at $d_h \sim$ 120−300 nm. Taking into account the obtained results from the cryo-TEM imaging (presented below), this result can be interpreted as a coexistence of small vesicular bilayer membranes and larger particles, e.g., precursors of cubosomes, spongosomes, or intermediate type structures and multi-architecture assemblies. Figures 9−13 well reveal the topological characteristics of such coexistences.

Compartmentalized Membranous Architectures Revealed by Cryo-TEM Imaging. The composition-dependent evolution of the nanocarrier morphologies during the spontaneous self-assembly process in the hydrated MO/EPA/DOPE-PEG_{2000} mixtures was directly visualized by cryogenic transmission electron microscopy (cryo-TEM). The performed imaging remarked the effect of the sample preparation procedure for the topology of the dispersed nanocarriers in addition to the major role of the molar ratio between the amphiphiles MO and EPA in the 3D nanoarchitecture formation. Figure 7a,b presents the morphology of the MO/

DOI: 10.1021/acsomega.7b01935
ACS Omega 2018, 3, 3235−3247

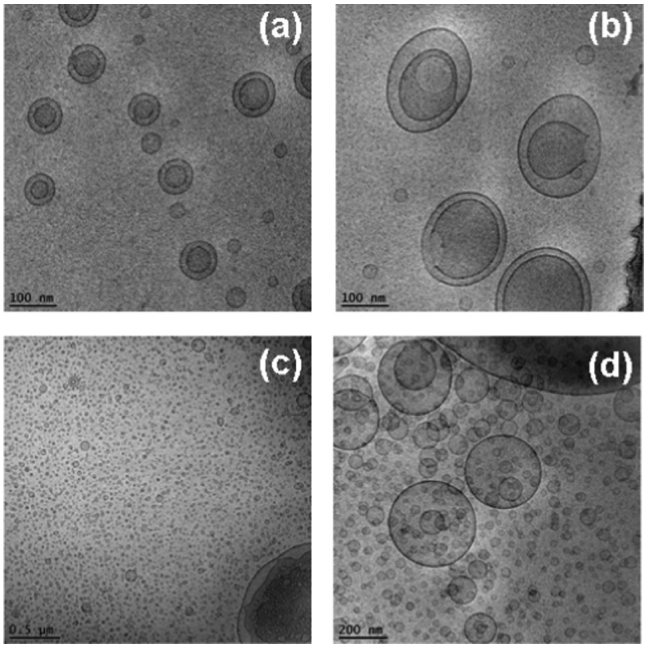

Figure 7. Cryo-TEM images of double membrane nanocarriers MO/DOPE-PEG_{2000} (98:2 mol/mol) obtained after sterile filtering using 0.2 μm pore-sized microporous membrane filters (a, b), and of MO/EPA/DOPE-PEG_{2000} carriers (MO/EPA ratio 70:30 mol/mol) dispersed to small vesicles through vigorous physical agitation (c, d).

DOPE-PEG_{2000} particles before the addition of EPA. After the passage through the 0.2 μm pore-sized filter membrane, the dispersed system contained double membrane vesicles, some of which were of a vase-like architecture. Small vesicular membrane objects were observed in the MO/EPA/DOPE-PEG_{2000} dispersions subjected to ultrasonication (Figure 7c,d). Owing to the fact that filtering of the samples removes the big objects of inner 3D lipid membrane organization, the majority of the studied liquid crystalline carriers were prepared by moderate sonication of the lipid mixtures in an ice bath. Figure 8 indicates that the sonication procedure may yield various nonequilibrium morphologies such as cubosomal precursors and perforated vesicular architectures in addition to unilamellar vesicles and double bilayer membrane containers. Upon storage, these precursor structures may fuse or rearrange toward the formation of stably existing self-assembled nanocarrier structures involving EPA (Figures 9–13).

Figure 9 shows cryo-TEM micrographs of cubosome particles obtained at MO/EPA ratio 80:20 (mol/mol) in the MO/EPA/DOPE-PEG_{2000} mixture. The performed fast Fourier transform of the image in Figure 9b confirmed the nonlamellar periodic internal structure of nanochannels inside the nanocarriers. The projected plane corresponds to a cubic lattice packing of a primitive type. In the excess aqueous medium, the well-shaped cubosomes coexisted with bilayer membrane vesicles and some intermediate type of nonlamellar structures at an MO/EPA ratio 85:15 (mol/mol) (Figure 9c).

At equal molar content of EPA and MO in the self-assembled mixture (50:50 mol/mol), the topology of the nonfiltered nanocarrier system involved particles with dense cores as well as mixed types of lipid containers (Figure 10). The cryo-TEM images showed a large fraction of dense nanoparticles. Moreover, Figure 10b reveals a nanocarrier of a mixed type, in which a dense oil-like compartment and a vesicular aqueous compartment are joint. The resulting interface is well visible.

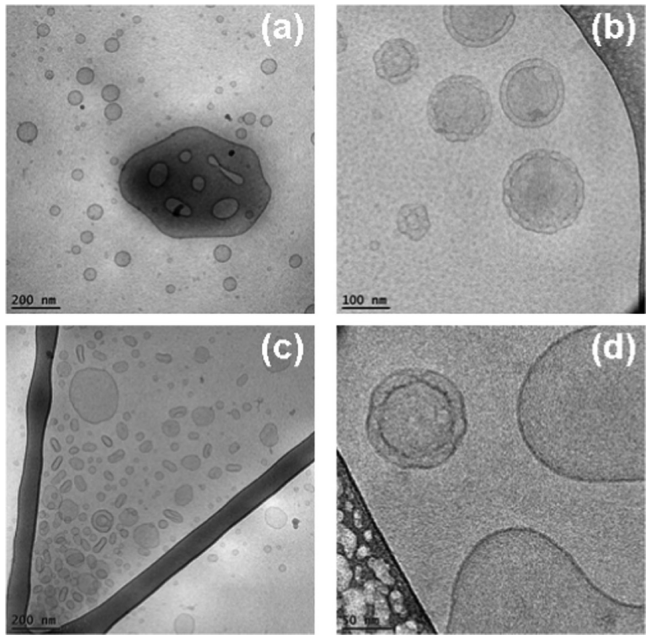

Figure 8. Cryo-TEM images of dispersed MO/EPA/DOPE-PEG_{2000} systems showing the unilamellar vesicles, perforated vesicular architectures, double bilayer membrane containers, and cubosomal precursors observed at MO/EPA ratios 85:15 mol/mol (a), 80:20 mol/mol (b, d), and 50:50 mol/mol (c) after sterile filtering of the samples. These objects may represent the populations of small particles detected in Figure 6a–c.

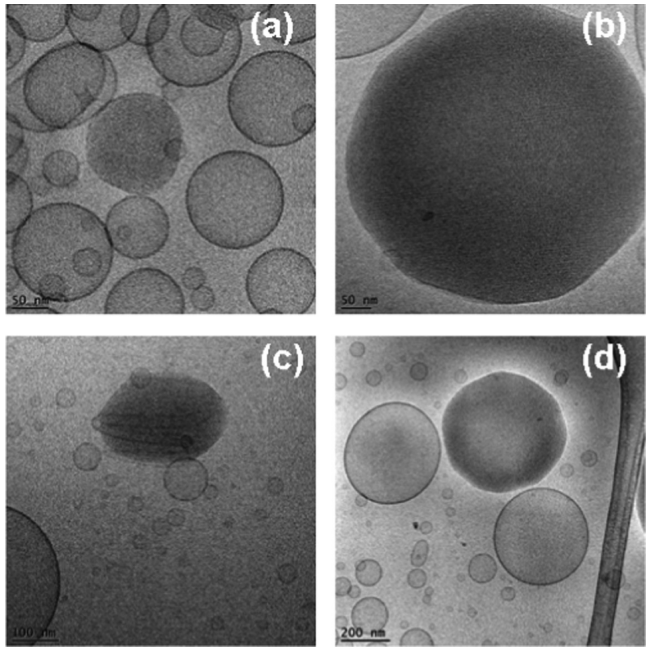

Figure 9. Cryo-TEM images of dispersed MO/EPA/DOPE-PEG_{2000} carriers (MO/EPA ratios 80:20 and 85:15 mol/mol) showing a coexistence of cubic membrane particles (cubosomes) (a, b, d), intermediate type of nonlamellar structures (c), and bilayer membrane vesicles (a–d). The aqueous medium contains the antioxidant BHT ensuring the oxidative stability of the formulations.

The presence of oil-rich droplets is indicative of the formation of EPA-rich nanodomains.

Figure 11 demonstrates a rich variety of topologies generated at an MO/EPA ratio of 40:60 (mol/mol) in the nonfiltered

DOI: 10.1021/acsomega.7b01935
ACS Omega 2018, 3, 3235–3247

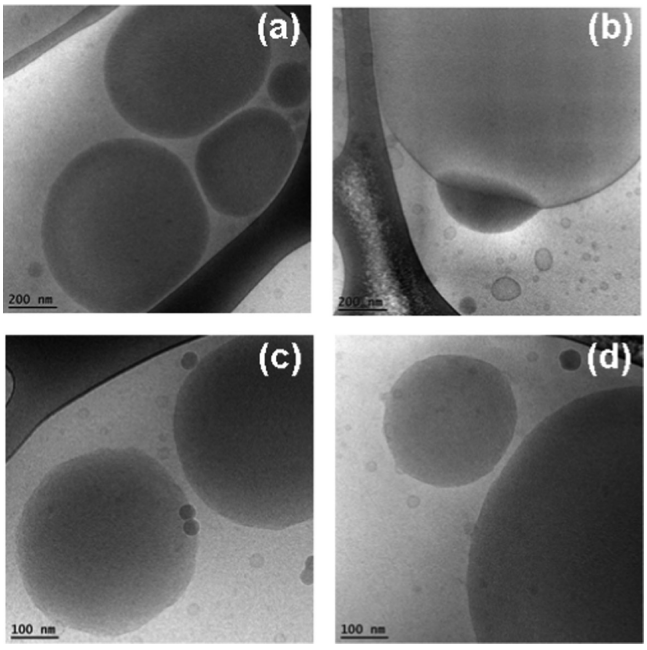

Figure 10. Cryo-TEM images of nanocarriers in MO/EPA/DOPE-PEG_{2000} dispersions at an MO/EPA ratio 50:50 (mol/mol). Dense particles (a, c, d) coexist with mixed objects built-up by an oil compartment joined to a vesicle (b). The dense particles can be cubosomes rich in EPA.

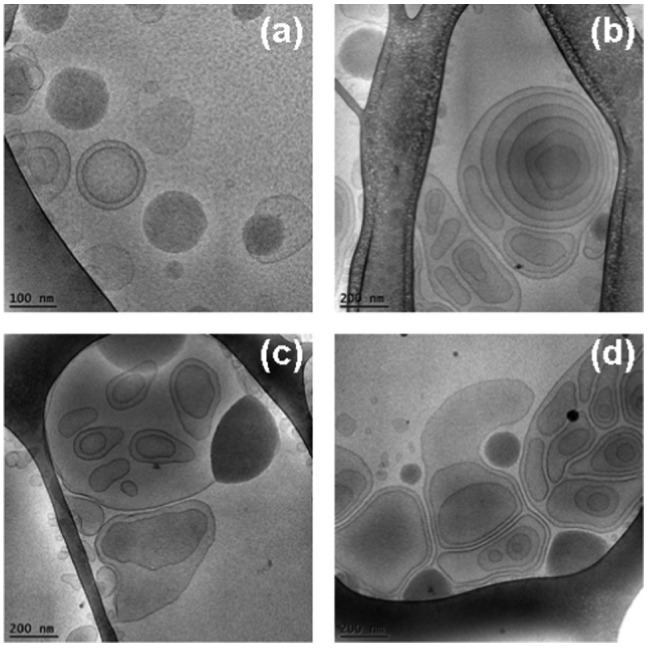

Figure 11. Cryo-TEM images of multiarchitecture assemblies (a–d) formed in the MO/EPA/DOPE-PEG_{2000} lipid system at a MO/EPA ratio 40:60 (mol/mol). The dispersed objects involve interfaces with uneven distributions of the membrane curvature. Lipid bilayers arranged in onionlike particles are also present.

MO/EPA/DOPE-PEG_{2000} dispersed system. The observed heterogeneity comprises vesicular membranes' morphologies with different genus, multilamellar liquid crystalline structures, precursors of spongosomes, and dense oil-like compartments (Figure 11a–d). Some of the nano-objects exhibited edges at their peripheries or at their inner compartments. The coexistence of liquid crystalline lipid membranous particles, of various topologies, with more dense structures of oil dropletlike morphology represents the inhomogeneous distribution of the membrane curvature at this amphiphilic composition. Although the MO membranes appear to be a good solubilization medium for the EPA molecules, the excess of EPA tends to form oil-rich nanodomains or compartments inside the carriers. Figure 11c demonstrates a mixed object consisting of an aqueous compartment, surrounded by a bilayer lipid membrane (vesicle) and an adjacent oil compartment rich in EPA. Such mixed type carriers may be of interest for combination therapies requiring encapsulation of both hydrosoluble and liposoluble drug molecules.

Figure 12 shows the nanocarrier topologies in the MO/EPA/DOPE-PEG_{2000} system at a molar ratio 30:70 (MO/EPA, mol/mol). The different panels display the possible stages of the perforation of the lipid membrane vesicles and their assembly into 3D structures. Mesoporous liquid crystalline architectures are generated starting from perforated vesicular membranes. The PEGylated vesicular particles are stabilized by double membrane peripheries, and their core gets perforated upon the formation of nanochanneled architectures. The compartmentalization of the membranous structures is done through interlamellar attachments between the bilayers. Figure 12 indicates how the varying degree of lipid membrane perforation results in a swollen-type nanosponge organization. The density of the aqueous channels in these carriers is low, whereas the channel size is large. We refer to these sponge-phase particles as spongosomes with large channels.

It should be noted that the insufficient quantity of the employed PEGylated agent provoked heterogeneous topologies of the spongosomes and hence differences in the nanochannels hydration. The performed cryo-TEM investigation established that the dispersed spongosome carriers (spongosomes with large channels) coexist with a weakly hydrated sponge-phase (Figure 13). The density of the aqueous nanochannels in this fraction of the liquid crystalline sample appears to be essentially higher as compared to that in Figure 12. We refer to this sponge-phase fraction as weakly hydrated spongosomes. The uneven distribution of the material yielded also nanosponges encapsulating oil-like nanodomains enriched in EPA (Figure 13d). Therefore, (i) swollen nanosponges with large aqueous channels, (ii) weakly hydrated sponges, and (iii) spongosomes encapsulating EPA nanodomains can be formed under the conditions of excess EPA fraction in the amphiphilic mixture. Higher EPA quantities in the mixtures may be expected to lead to phase separation of microscopic oil-phase fractions.

All samples in the present work were prepared at pH 7. The pH sensitivity of the mixed EPA/MO lipid assemblies was out of the scope of our study. Nevertheless, this topic is of considerable interest for applications employing stimulus-responsive nanocarriers.[13,34,55−57] It is known that the pK_a of unsaturated fatty acids in lipidic or protein environment is shifted with regard to the pK_a of the carboxyl (COOH) groups in aqueous solution phase.[104−106] Depending on the experimental system, the pH for the onset of interfacial ionization of the COOH groups needs to be particularly examined, as it depends on the fatty acid chain length, unsaturation, and the concentration and type of the counterions in the aqueous phase. Although the pK_a is about 5 for carboxyl groups in a bulk aqueous solution, this value can be substantially higher for interfacially exposed COOH groups. Owing to the lower dielectric constant of the lipid headgroup environment,[107] the

DOI: 10.1021/acsomega.7b01935
ACS Omega 2018, 3, 3235−3247

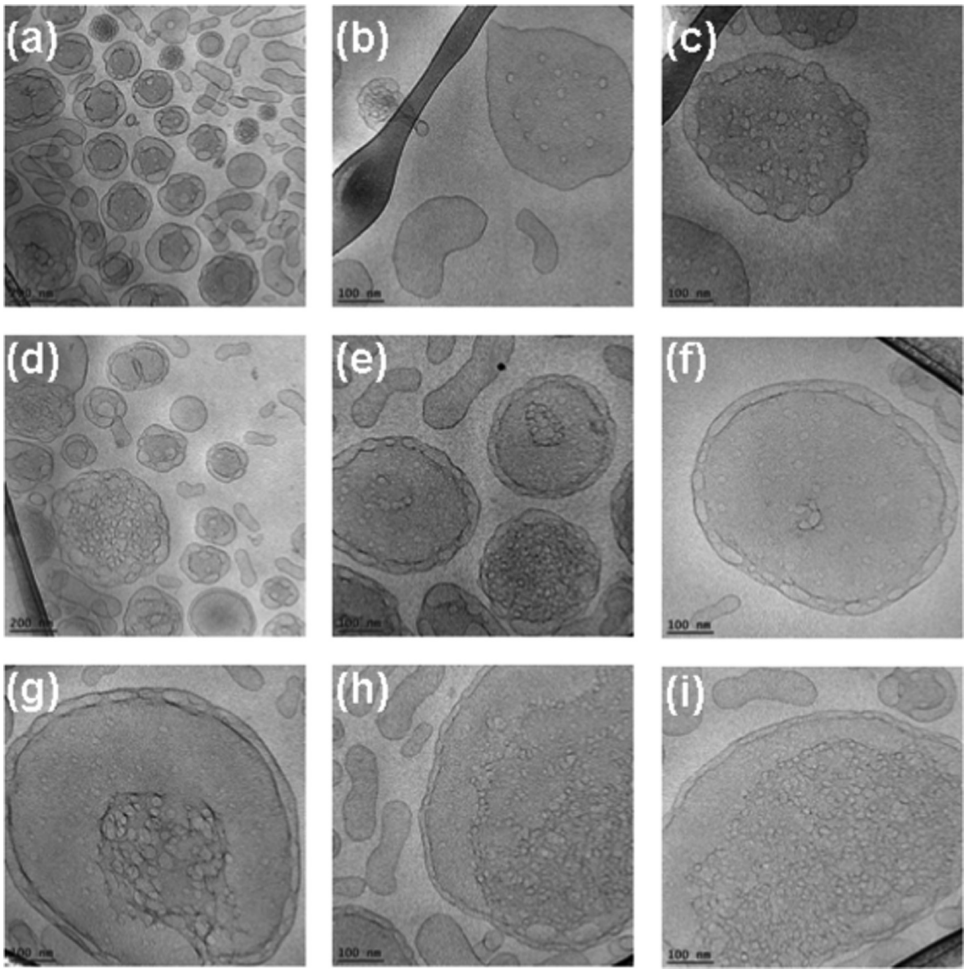

Figure 12. Cryo-TEM images of nanosponge particles generated at an MO/EPA ratio 30:70 (mol/mol) and stabilized by 2 mol % DOPE-PEG$_{2000}$. The aqueous dispersion contains spongosome carriers with different degrees of membrane perforation, which yields swollen sponge membrane type inner organization of the particles (a–i).

pK_a value is about 7 for COOH groups in the interfacial region.[104,105] The apparent pK_a for the PUFAs[106] is close to the physiological pH. Under these conditions, the ionization state may influence the critical packing parameter (CPP) of the lipid mixtures in which PUFA is involved. Previous reports[55] have exploited the fact that the increase of pH may decrease the CPP of the amphiphilic assemblies owing to the ionization of the headgroups. Although pH was not varied in our system, the obtained structural results indicated a transition to less curved membrane structures at higher PUFA content, which is associated with the decreased hydration of the lipid/water interfaces and the sizes of the aqueous compartments. These effects might be related to the ionization state of the EPA headgroups at the lipid membrane interfaces and require future work toward the design of controlled release nanoassemblies.

CONCLUSIONS

In this work, we obtained new knowledge about the structural properties of the ω-3 polyunsaturated fatty acid EPA at microscopic and nanoscale levels. Whereas ω-3 PUFAs present strong interest as bioactive lipids, the established self-assembly behavior of EPA revealed that it requires colipids or coamphiphiles for the formation of stable liquid crystalline nanoparticulate dispersions of therapeutic significance. The performed SAXS investigation resolved intermediate states induced upon composition-mediated curvature changes in the self-assembled membranes with MO. A phase transition from a periodic to a random organization of the EPA-embedding lipid membranes was detected. The cryo-TEM imaging established that the encapsulation of EPA strongly influences the inner liquid crystalline organization of the carriers at the nanoscale. The multiarchitecture assemblies comprise topological features of double membrane vesicles, cubosomes, spongosomes, and their precursors. Inhomogeneous membrane curvature distribution was observed at elevated molar fractions of EPA. Bicompartment nano-objects with joint vesicle and oil compartments were also found as a function of the MO/EPA molar ratio. Highly swollen spongosomes and weakly hydrated nanosponges were produced with the investigated MO/EPA/DOPE-PEG$_{2000}$ systems depending on the experimental conditions.

In our opinion, an interesting result for future therapeutic applications might be the stealth spongosomes and nanosponges formed at an MO/EPA ratio 30:70 (mol/mol). They contain a large fraction of bioactive lipid (ω-3 PUFA) with regard to the helper lipid (MO). In perspective, it may be considered that the structural organization of such hydrated lipid sponges may be suitable for preparation of nanocarriers combining water-insoluble and water-soluble drugs in their multicompartment architecture.

DOI: 10.1021/acsomega.7b01935
ACS Omega 2018, 3, 3235–3247

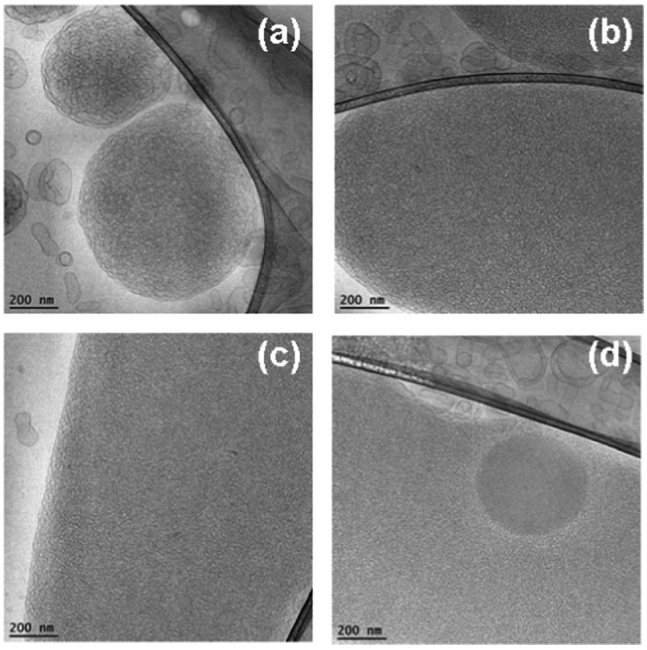

Figure 13. Cryo-TEM images of weakly hydrated spongosomes (a, b) and of sponge-phase nanocarriers with high density of aqueous channels (c, d) in the MO/EPA/DOPE-PEG_{2000} system (MO/EPA ratio 30:70). The dense droplet in image (d) likely corresponds to an EPA-rich nanodomain encapsulated in the nanosponge of a mixed composition.

EXPERIMENTAL SECTION

Materials and Sample Preparation. *cis*-5,8,11,14,17-Eicosapentaenoic acid (20:5, EPA) and 1-monooleoyl-*rac*-glycerol (MO) [C18:1c9, MW 356.54, powder, purity 99.5%] were purchased from Sigma-Aldrich (France). The PEGylated phospholipid 1,2-dioleoyl-*sn*-glycero-3-phosphoethanolamine-*N*-(methoxy(poly(ethylene glycol))-2000) ammonium salt (DOPE-PEG_{2000}) (MW 2801.51 g/mol) was purchased from Avanti Polar Lipids (Coger, Paris, France). A phosphate buffer solution (NaH_2PO_4/Na_2HPO_4, 1×10^{-2} M, pH 7, p.a. grade, Merck) was prepared using Milli-Q water (Millipore Co.). It contained small amounts of the antioxidant butylated hydroxytoluene (BHT).

Bulk phases and dispersed liquid crystalline carriers were obtained by the method of hydration of a dry lipid film followed by physical agitation. Chloroform solutions of MO and EPA were mixed at varying ratios of 90:10, 85:15, 80:20, 70:30, 50:50, 40:60, and 30:70 (mol/mol). The phospholipid DOPE-PEG_{2000} was added (2 mol % with regard to MO) in the amphiphilic mixtures, which required dispersion into nanovehicles. After mixing of the lipid components, the solvent was evaporated from the MO/EPA and the MO/EPA/DOPE-PEG_{2000} samples under a gentle stream of nitrogen gas to obtain fine and homogeneous lipid films, which were lyophilized overnight. The hydration of the mixed lipid layers was performed by incubation with a BHT-containing phosphate buffer solution at room temperature. Bulk phases were self-assembled in 60 wt % aqueous phase. Nanoparticulate dispersions were obtained in 95 wt % excess aqueous phase by vortexing and agitation in an ice bath. Ultrasonic cycles with a total duration of about 20 min (Branson 2510 ultrasonic bath, "set sonics" mode, power 60 W) were performed. Filtration of the dispersions through 0.2 μm pore-sized microporous membrane filters (Minisart High Flow, Sartorius) was performed under a laminar flow hood.

Synchrotron SAXS. Synchrotron SAXS experiments were performed at the P12 BioSAXS beamline[108] of the European Molecular Biology Laboratory (EMBL) at the storage ring PETRA III of the Deutsche Elektronen Synchrotron (DESY, Hamburg, Germany) at 20 °C using a Pilatus 2M detector (1475 pixels × 1679 pixels) (Dectris, Switzerland) and synchrotron radiation with a wavelength λ = 1 Å. The sample-to-detector distance was 3 m, allowing for measurements in the q-range interval from 0.01 to 0.44 $Å^{-1}$. The q-vector was defined as $q = (4\pi/\lambda)\sin\theta$, where 2θ is the scattering angle. The q-range was calibrated using the diffraction patterns of silver behenate. The experimental data were normalized with respect to the transmitted beam intensity and corrected for nonhomogeneous detector response. The background scattering of the quartz capillary and the aqueous buffer was subtracted. The aqueous buffer scattering was measured before and after every sample scattering to control for eventual sample holder contamination. Twenty consecutive frames (each of 0.05 s) comprising the measurements for the sample and the solvent were acquired. No measurable radiation damage was detected by the comparison of the frames. The final scattering curve was obtained using the program PRIMUS by averaging the scattering data collected from the different frames. An automatic sample changer adjusted for sample volume of 20 μL and a filling cycle of 1 min was used.

Cryogenic Transmission Electron Microscopy (Cryo-TEM). For cryo-TEM studies, a sample droplet of 2 μL was put on a lacey carbon film-covered copper grid (Science Services, Munich, Germany), which was hydrophilized by glow discharge (Solarus, Gatan, Munich, Germany) for 30 s. Most of the liquid was then removed with blotting paper, leaving a thin film stretched over the lace holes. The specimen was instantly shock frozen by rapid immersion into liquid ethane and cooled to approximately 90 K by liquid nitrogen in a temperature-and-humidity-controlled freezing unit (Leica EMGP, Wetzlar, Germany). The temperature and humidity were monitored and kept constant in the chamber during all sample preparation steps. The specimen was inserted into a cryo transfer holder (CT3500; Gatan, Munich, Germany) and transferred to a Zeiss EM922 Omega energy-filtered TEM (EFTEM) instrument (Carl Zeiss Microscopy, Jena, Germany). Examinations were carried out at temperatures around 90 K. The TEM instrument was operated at an acceleration voltage of 200 kV. Zero-loss-filtered images (DE = 0 eV) were taken under reduced dose conditions (100−1000 e/nm^2). The images were recorded digitally by a bottom-mounted charge-coupled device camera system (Ultra Scan 1000; Gatan, Munich, Germany) and combined and processed with a digital imaging processing system (Digital Micrograph GMS 1.9; Gatan, Munich, Germany). The sizes of the investigated nanoparticles were in the range or below the film thickness, and no deformations were observed. The images were taken very close to focus or slightly under the focus (some nanometers) due to the contrast enhancing capabilities of the in-column filter of the employed Zeiss EM922 Omega. In EFTEMs, deep underfocused images can be totally avoided.

Polarized Optical Microscopy (POM). Thin films of bulk liquid crystalline phase samples were studied under cross polarizers by POM using cells of two cover glass slides inserted in a temperature-controlled stage. The experimental setup included a microscope Nikon Eclipse E600 equipped with a

DOI: 10.1021/acsomega.7b01935
ACS Omega 2018, 3, 3235−3247

polarizer and a Mightex Buffer USB camera (Mightex Systems). Objectives with magnifications of 10×, 20×, and 40× were employed.

Quasielastic Light Scattering (QELS). The particle sizes in the investigated lipid dispersions were determined using a Nanosizer apparatus (Nano-ZS90; MALVERN) equipped with a helium−neon laser of 633 nm wavelength. The nanocarriers were suspended in a buffer solution in 1 cm thick cells and analyzed in a manual mode using the following experimental parameters: temperature, 25 °C; scattering angle, 90°; refracting index, 1.33; and environment medium viscosity, 0.890 cP. The average hydrodynamic diameter, d_h, was calculated considering the mean translational diffusion coefficient, D, of the particles in accordance with the Stokes−Einstein law for spherical particles in the absence of interactions: $d_h = k_B T/3\eta\pi D$, where k_B is the Boltzmann constant, T is the temperature, and η is the viscosity of the aqueous medium. The results were analyzed using MALVERN Zetasizer software. The particle distribution by size was expressed in the "volume" analysis configuration after averaging three measurements with the same sample. The plotted maximal intensities correspond to the mean nano-object sizes, which are most abundant in the sample volume.

AUTHOR INFORMATION

Corresponding Author

*E-mail: Angelina.Angelova@u-psud.fr.

ORCID

Angelina Angelova: 0000-0002-0285-0637

Notes

The authors declare no competing financial interest.

ACKNOWLEDGMENTS

The synchrotron SAXS data were collected at beamline P12 operated by EMBL Hamburg at the PETRA III storage ring of DESY (Deutsche Elektronen Synchrotron, Hamburg, Germany). We would like to thank C.E. Blanchet for the assistance in using the beamline. B.A. is supported by the Czech Science Foundation Grant GACR 17-00973S and the European Commission funded projects ELI, Extreme Light Infrastructure, phase 2 (CZ.02.1.01/0.0/0.0/15_008/0000162) and ELIBIO (CZ.02.1.01/0.0/0.0/15_003/0000447) from the European Regional Development Fund. M.D. is supported by the collaborative research centre SFB840 of the German Science Foundation DFG.

REFERENCES

(1) Björnmalm, M.; Faria, M.; Caruso, F. Increasing the impact of materials in and beyond bio-nano science. *J. Am. Chem. Soc.* **2016**, *138*, 13449−13456.

(2) Yoo, J. W.; Irvine, D. J.; Discher, D. E.; Mitragotri, S. Bio-inspired, bioengineered and biomimetic drug delivery carriers. *Nat. Rev. Drug Discovery* **2011**, *10*, 521−535.

(3) Azmi, I. D.; Wibroe, P. P.; Wu, L. P.; Kazem, A. I.; Amenitsch, H.; Moghimi, S. M.; Yaghmur, A. A structurally diverse library of safe-by-design citrem-phospholipid lamellar and non-lamellar liquid crystalline nano-assemblies. *J. Controlled Release* **2016**, *239*, 1−9.

(4) Kirkensgaard, J. J. K.; Evans, M. E.; de Campo, L.; Hyde, S. T. Hierarchical self-assembly of a striped gyroid formed by threaded chiral mesoscale networks. *Proc. Natl. Acad. Sci. U.S.A.* **2014**, *111*, 1271−1276.

(5) de Campo, L.; Castle, T.; Hyde, S. T. Optimal packings of three-arm star polyphiles: from tricontinuous to quasi-uniformly striped bicontinuous forms. *Interface Focus* **2017**, *7*, No. 20160130.

(6) Boyd, B. J.; Dong, Y.-D.; Rades, T. Nonlamellar liquid crystalline nanostructured particles: Advances in materials and structure determination. *J. Liposome Res.* **2009**, *19*, 12−23.

(7) Hoppel, M.; Caneri, M.; Glatter, O.; Valenta, C. Self-assembled nanostructured aqueous dispersions as dermal delivery systems. *Int. J. Pharm.* **2015**, *495*, 459−462.

(8) Ariga, K.; Li, J.; Fei, J.; Ji, Q.; Hill, J. P. Nanoarchitectonics for dynamic functional materials from atomic-/molecular-level manipulation to macroscopic action. *Adv. Mater.* **2016**, *28*, 1251−1286.

(9) Angelova, A.; Angelov, B.; Mutafchieva, R.; Lesieur, S.; Couvreur, P. Self-assembled multicompartment liquid crystalline lipid carriers for protein, peptide, and nucleic acid drug delivery. *Acc. Chem. Res.* **2011**, *44*, 147−156.

(10) Nilsson, C.; Østergaard, J.; Larsen, S. W.; Larsen, C.; Urtti, A.; Yaghmur, A. PEGylation of phytantriol-based lyotropic liquid crystalline particles - the effect of lipid composition, PEG chain length, and temperature on the internal nanostructure. *Langmuir* **2014**, *30*, 6398−6407.

(11) Angelova, A.; Angelov, B.; Garamus, V. M.; Couvreur, P.; Lesieur, S. Small-angle X-ray scattering investigations of biomolecular confinement, loading, and release from liquid-crystalline nanochannel assemblies. *J. Phys. Chem. Lett.* **2012**, *3*, 445−457.

(12) Gallová, J.; Uhríková, D.; Kučerka, N.; Doktorovová, S.; Funari, S. S.; Teixeira, J.; Balgavý, P. The effects of cholesterol and β-sitosterol on the structure of saturated diacylphosphatidylcholine bilayers. *Eur. Biophys. J.* **2011**, *40*, 153−163.

(13) Aleandri, S.; Speziale, C.; Mezzenga, R.; Landau, E. M. Design of light-triggered lyotropic liquid crystal mesophases and their application as molecular switches in 'On demand' release. *Langmuir* **2015**, *31*, 6981−6987.

(14) Angelova, A.; Angelov, B. Dual and multi-drug delivery nanoparticles towards neuronal survival and synaptic repair. *Neural Regener. Res.* **2017**, *12*, 886−889.

(15) Esposito, E.; Drechsler, M.; Mariani, P.; Panico, A. M.; Cardile, V.; Crascì, L.; Carducci, F.; Graziano, A. C. E.; Cortesi, R.; Puglia, C. Nanostructured lipid dispersions for topical administration of crocin, a potent antioxidant from saffron (*Crocus sativus* L.). *Mater. Sci. Eng., C* **2017**, *71*, 669−677.

(16) Boge, L.; Bysell, H.; Ringstad, L.; Wennman, D.; Umerska, A.; Cassisa, V.; Eriksson, J.; Joly-Guillou, M. L.; Edwards, K.; Andersson, M. Lipid-based liquid crystals as carriers for antimicrobial peptides: Phase behavior and antimicrobial effect. *Langmuir* **2016**, *32*, 4217−4228.

(17) Angelova, A.; Angelov, B.; Mutafchieva, R.; Lesieur, S. Biocompatible mesoporous and soft nanoarchitectures. *J. Inorg. Organomet. Polym. Mater.* **2015**, *25*, 214−232.

(18) Tran, N.; Mulet, X.; Hawley, A. M.; Conn, C. E.; Zhai, J.; Waddington, L. J.; Drummond, C. J. First direct observation of stable internally ordered Janus nanoparticles created by lipid self-assembly. *Nano Lett.* **2015**, *15*, 4229−4233.

(19) Shrestha, R. G.; Abezgauz, L.; Danino, D.; Sakai, K.; Sakai, H.; Abe, M. Structure and dynamics of poly(oxyethylene) cholesteryl ether wormlike micelles: rheometry, SAXS, and cryo-TEM studies. *Langmuir* **2011**, *27*, 12877−12883.

(20) Tran, T.; Siqueira, S. D. V. S.; Amenitsch, H.; Rades, T.; Müllertz, A. Monoacyl phosphatidylcholine inhibits the formation of lipid multilamellar structures during in vitro lipolysis of self-emulsifying drug delivery systems. *Eur. J. Pharm. Sci.* **2017**, *108*, 62−70.

(21) Hyde, S. Identification of Lyotropic Liquid Crystalline Mesophases. In *Handbook of Applied Surface and Colloid Chemistry*; Holmberg, K., Ed.; John Wiley & Sons: Chichester, U.K., 2002; pp 299−320.

(22) Chang, D. P.; Jankunec, M.; Barauskas, J.; Tiberg, F.; Nylander, T. Adsorption of lipid liquid crystalline nanoparticles: effects of

DOI: 10.1021/acsomega.7b01935
ACS Omega 2018, 3, 3235−3247

particle composition, internal structure, and phase behavior. *Langmuir* **2012**, *28*, 10688−10696.
(23) Bastos, M.; Silva, T.; Teixeira, V.; Nazmi, K.; Bolscher, J. G.; Funari, S. S.; Uhríková, D. Lactoferrin-derived antimicrobial peptide induces a micellar cubic phase in a model membrane system. *Biophys. J.* **2011**, *101*, L20−L22.
(24) Nilsson, C.; Barrios-Lopez, B.; Kallinen, A.; Laurinmäki, P.; Butcher, S. J.; Raki, M.; Weisell, J.; Bergström, K.; Larsen, S. W.; Østergaard, J.; Larsen, C.; Urtti, A.; Airaksinen, A. J.; Yaghmur, A. SPECT/CT imaging of radiolabeled cubosomes and hexosomes for potential theranostic applications. *Biomaterials* **2013**, *34*, 8491−8503.
(25) Wadsäter, M.; Barauskas, J.; Nylander, T.; Tiberg, F. Formation of highly structured cubic micellar lipid nanoparticles of soy phosphatidylcholine and glycerol dioleate and their degradation by triacylglycerol lipase. *ACS Appl. Mater. Interfaces* **2014**, *6*, 7063−7069.
(26) Angelov, B.; Angelova, A.; Filippov, S. K.; Drechsler, M.; Štěpánek, P.; Lesieur, S. Multicompartment lipid cubic nanoparticles with high protein upload: Millisecond dynamics of formation. *ACS Nano* **2014**, *8*, 5216−5226.
(27) Zhai, J.; Tran, N.; Sarkar, S.; Fong, C.; Mulet, X.; Drummond, C. J. Self-assembled lyotropic liquid crystalline phase behavior of monoolein−capric acid−phospholipid nanoparticulate systems. *Langmuir* **2017**, *33*, 2571−2580.
(28) Angelov, B.; Angelova, A.; Garamus, V. M.; Drechsler, M.; Willumeit, R.; Mutafchieva, R.; Štěpánek, P.; Lesieur, S. Earliest stage of the tetrahedral nanochannel formation in cubosome particles from unilamellar nanovesicles. *Langmuir* **2012**, *28*, 16647−16655.
(29) Akhlaghi, S. P.; Ribeiro, I. R.; Boyd, B. J.; Loh, W. Impact of preparation method and variables on the internal structure, morphology, and presence of liposomes in phytantriol-Pluronic() F127 cubosomes. *Colloids Surf., B* **2016**, *145*, 845−853.
(30) Efrat, R.; Kesselman, E.; Aserin, A.; Garti, N.; Danino, D. Solubilization of hydrophobic guest molecules in the monoolein discontinuous QL cubic mesophase and its soft nanoparticles. *Langmuir* **2009**, *25*, 1316−1326.
(31) Góźdź, W. T. Cubosome topologies at various particle sizes and crystallographic symmetries. *Langmuir* **2015**, *31*, 13321−13326.
(32) Yaghmur, A.; de Campo, L.; Sagalowicz, L.; Leser, M. E.; Glatter, O. Control of the internal structure of MLO-based isasomes by the addition of diglycerol monooleate and soybean phosphatidylcholine. *Langmuir* **2006**, *22*, 9919−9927.
(33) Angelov, B.; Angelova, A.; Drechsler, M.; Garamus, V. M.; Mutafchieva, R.; Lesieur, S. Identification of large channels in cationic PEGylated cubosome nanoparticles by synchrotron radiation SAXS and Cryo-TEM imaging. *Soft Matter* **2015**, *11*, 3686−3692.
(34) Nazaruk, E.; Szlęzak, M.; Górecka, E.; Bilewicz, R.; Osornio, Y. M.; Uebelhart, P.; Landau, E. M. Design and assembly of pH-sensitive lipidic cubic phase matrices for drug release. *Langmuir* **2014**, *30*, 1383−1390.
(35) Aleandri, S.; Bandera, D.; Mezzenga, R.; Landau, E. M. Biotinylated cubosomes: A versatile tool for active targeting and codelivery of paclitaxel and a fluorescein-based lipid dye. *Langmuir* **2015**, *31*, 12770−12776.
(36) Han, S.; Shen, J. Q.; Gan, Y.; Geng, H. M.; Zhang, X. X.; Zhu, C. L.; Gan, L. Novel vehicle based on cubosomes for ophthalmic delivery of flurbiprofen with low irritancy and high bioavailability. *Acta Pharmacol. Sin.* **2010**, *31*, 990−998.
(37) Shen, H. H.; Lake, V.; Le Brun, A. P.; James, M.; Duff, A. P.; Peng, Y.; McLean, K. M.; Hartley, P. G. Targeted detection of phosphatidylserine in biomimetic membranes and in vitro cell systems using annexin V-containing cubosomes. *Biomaterials* **2013**, *34*, 8361−8369.
(38) Neto, C.; Giovanni Aloisi, G.; Baglioni, P.; Larsson, K. Imaging soft matter with the atomic force microscope: Cubosomes and hexosomes. *J. Phys. Chem. B* **1999**, *103*, 3896−3899.
(39) Nilsson, C.; Edwards, K.; Eriksson, J.; Larsen, S. W.; Østergaard, J.; Larsen, C.; Urtti, A.; Yaghmur, A. Characterization of oil-free and oil-loaded liquid-crystalline particles stabilized by negatively charged stabilizer citrem. *Langmuir* **2012**, *28*, 11755−11766.
(40) Boyd, B. J.; Rizwan, S. B.; Dong, Y. D.; Hook, S.; Rades, T. Self-assembled geometric liquid-crystalline nanoparticles imaged in three dimensions: Hexosomes are not necessarily flat hexagonal prisms. *Langmuir* **2007**, *23*, 12461−12464.
(41) Oka, T.; Ohta, N. Two distinct cylinder arrangements in monodomains of a lyotropic liquid crystalline hexagonal II phase: Monodomains with straight cylinders and ringed cylinders in capillaries. *Langmuir* **2016**, *32*, 7613−7620.
(42) Angelov, B.; Garamus, V. M.; Drechsler, M.; Angelova, A. Structural analysis of nanoparticulate carriers for encapsulation of macromolecular drugs. *J. Mol. Liq.* **2017**, *235*, 83−89.
(43) Rodrigues, L.; Kyriakos, K.; Schneider, F.; Dietz, H.; Winter, G.; Papadakis, C. M.; Hubert, M. Characterization of lipid-based hexosomes as versatile vaccine carriers. *Mol. Pharmaceutics* **2016**, *13*, 3945−3954.
(44) Bye, N.; Hutt, O. E.; Hinton, T. M.; Acharya, D. P.; Waddington, L. J.; Moffat, B. A.; Wright, D. K.; Wang, H. X.; Mulet, X.; Muir, B. W. Nitroxide-loaded hexosomes provide MRI contrast in vivo. *Langmuir* **2014**, *30*, 8898−8906.
(45) Valldeperas, M.; Wiśniewska, M.; Ram-On, M.; Kesselman, E.; Danino, D.; Nylander, T.; Barauskas, J. Sponge phases and nanoparticle dispersions in aqueous mixtures of mono- and diglycerides. *Langmuir* **2016**, *32*, 8650−8659.
(46) Angelov, B.; Angelova, A.; Mutafchieva, R.; Lesieur, S.; Vainio, U.; Garamus, V. M.; Jensen, G. V.; Pedersen, J. S. SAXS investigation of a cubic to a sponge (L3) phase transition in self-assembled lipid nanocarriers. *Phys. Chem. Chem. Phys.* **2011**, *13*, 3073−3081.
(47) Chen, Y.; Angelova, A.; Angelov, B.; Drechsler, M.; Garamus, V. M.; Willumeit-Römer, R.; Zou, A. Sterically stabilized spongosomes for multi-drug delivery of anticancer nanomedicines. *J. Mater. Chem. B* **2015**, *3*, 7734−7744.
(48) Zou, A.; Li, Y.; Chen, Y.; Angelova, A.; Garamus, V. M.; Li, N.; Drechsler, M.; Angelov, B.; Gong, Y. Self-assembled stable sponge-type nanocarries for *Brucea javanica* oil delivery. *Colloids Surf., B* **2017**, *153*, 310−319.
(49) Jang, Y.; Chung, H. J.; Hong, J. W.; Yun, C. W.; Chung, H. Absorption mechanism of DHP107, an oral paclitaxel formulation that forms a hydrated lipidic sponge phase. *Acta Pharmacol. Sin.* **2017**, *38*, 133−145.
(50) Hazzah, H. A.; Farid, R. M.; Nasra, M. M. A.; El-Massik, M. A.; Abdallah, O. Y. Lyophilized sponges loaded with curcumin solid lipid nanoparticles for buccal delivery: development and characterization. *Int. J. Pharm.* **2015**, *492*, 248−257.
(51) Kulkarni, C. V.; Yaghmur, A.; Steinhart, M.; Kriechbaum, M.; Rappolt, M. Effects of high pressure on internally self-assembled lipid nanoparticles: A synchrotron small-angle X-ray scattering (SAXS) study. *Langmuir* **2016**, *32*, 11907−11917.
(52) de Campo, L.; Yaghmur, A.; Sagalowicz, L.; Leser, M. E.; Watzke, H.; Glatter, O. Reversible phase transitions in emulsified nanostructured lipid systems. *Langmuir* **2004**, *20*, 5254−5261.
(53) Yaghmur, A.; Al-Hosayni, S.; Amenitsch, H.; Salentinig, S. Structural investigation of bulk and dispersed inverse lyotropic hexagonal liquid crystalline phases of eicosapentaenoic acid monoglyceride. *Langmuir* **2017**, *33*, 14045−14057.
(54) Huang, Z.; Epand, R. M. Study of the phase behaviour of fully hydrated saturated diacyl phosphatidylserine/fatty acid mixtures with 31P-NMR and calorimetry. *Chem. Phys. Lipids* **1997**, *86*, 161−169.
(55) Salentinig, S.; Sagalowicz, L.; Glatter, O. Self-assembled structures and pKa value of oleic acid in systems of biological relevance. *Langmuir* **2010**, *26*, 11670−11679.
(56) Negrini, R.; Mezzenga, R. pH-responsive lyotropic liquid crystals for controlled drug delivery. *Langmuir* **2011**, *27*, 5296−5303.
(57) Nakano, M.; Teshigawara, T.; Sugita, A.; Leesajakul, W.; Taniguchi, A.; Kamo, T.; Matsuoka, H.; Handa, T. Dispersions of liquid crystalline phases of the monoolein/oleic acid/Pluronic F127 system. *Langmuir* **2002**, *18*, 9283−9288.
(58) Bazinet, R. P.; Layé, S. Polyunsaturated fatty acids and their metabolites in brain function and disease. *Nat. Rev. Neurosci.* **2014**, *15*, 771−785.

DOI: 10.1021/acsomega.7b01935
ACS Omega 2018, 3, 3235−3247

(59) Cutuli, D. Functional and structural benefits induced by omega-3 polyunsaturated fatty acids during aging. *Curr. Neuropharmacol.* **2017**, *15*, 534−542.
(60) Bowen, K. J.; Harris, W. S.; Kris-Etherton, P. M. Omega-3 fatty acids and cardiovascular disease: Are there benefits? *Curr. Treat. Options Cardiovasc. Med.* **2016**, *18*, 69.
(61) Pinot, M.; Vanni, S.; Pagnotta, S.; Lacas-Gervais, S.; Payet, L.-A.; Ferreira, T.; Gautier, R.; Goud, B.; Antonny, B.; Barelli, H. Polyunsaturated phospholipids facilitate membrane deformation and fission by endocytic proteins. *Science* **2014**, *345*, 693−697.
(62) Feller, S. E.; Gawrisch, K.; MacKerell, A. D. Polyunsaturated fatty acids in lipid bilayers: intrinsic and environmental contributions to their unique physical properties. *J. Am. Chem. Soc.* **2002**, *124*, 318−326.
(63) Deng, Y.; Almsherqi, Z. A.; Shui, G.; Wenk, M. R.; Kohlwein, S. D. Docosapentaenoic acid (DPA) is a critical determinant of cubic membrane formation in amoeba Chaos mitochondria. *FASEB J.* **2009**, *23*, 2866−2871.
(64) Chong, K.; Deng, Y. The three dimensionality of cell membranes: lamellar to cubic membrane transition as investigated by electron microscopy. *Methods Cell Biol.* **2012**, *108*, 317−343.
(65) Levental, K. R.; Lorent, J. H.; Lin, X.; Skinkle, A. D.; Surma, M. A.; Stockenbojer, E. A.; Gorfe, A. A.; Levental, I. Polyunsaturated lipids regulate membrane domain stability by tuning membrane order. *Biophys. J.* **2016**, *110*, 1800−1810.
(66) Angelov, B.; Angelova, A. Nanoscale clustering of the neurotrophin receptor TrkB revealed by super-resolution STED microscopy. *Nanoscale* **2017**, *9*, 9797−9804.
(67) Shaikh, S. R.; Rockett, B. D.; Salameh, M.; Carraway, K. Docosahexaenoic acid modifies the clustering and size of lipid rafts and the lateral organization and surface expression of MHC class I of EL4 cells. *J. Nutr.* **2009**, *139*, 1632−1639.
(68) Shaikh, S. R. Biophysical and biochemical mechanisms by which dietary N-3 polyunsaturated fatty acids from fish oil disrupt membrane lipid rafts. *J. Nutr. Biochem.* **2012**, *23*, 101−105.
(69) Urquhart, R.; Chan, R. Y.; Li, O. T.; Tilley, L.; Grieser, F.; Sawyer, W. H. Omega-6 and omega-3 fatty acids: monolayer packing and effects on bilayer permeability and cholesterol exchange. *Biochem. Int.* **1992**, *26*, 831−841.
(70) Ehringer, W.; Belcher, D.; Wassall, S.; Stillwell, W. A comparison of the effects of linolenic (18:3) and docosahexaenoic (22:6) acids on phospholipid bilayers. *Chem. Phys. Lipids* **1990**, *54*, 79−88.
(71) Dumaual, A. C.; Jenski, L. J.; Stillwell, W. Liquid crystalline/gel state phase separation in docosahexaenoic acid-containing bilayers and monolayers. *Biochim. Biophys. Acta* **2000**, *1463*, 395−406.
(72) Wassall, S. R.; Stillwell, W. Docosahexaenoic acid domains: the ultimate non-raft membrane domain. *Chem. Phys. Lipids* **2008**, *153*, 57−63.
(73) Talbot, W. A.; Zheng, L.; Lentz, B. R. Acyl chain unsaturation and vesicle curvature alter outer leaflet packing and promote poly(ethylene glycol)-mediated membrane fusion. *Biochemistry* **1997**, *36*, 5827−5836.
(74) Haque, M. E.; McIntosh, T. J.; Lentz, B. R. Influence of lipid composition on physical properties and PEG-mediated fusion of curved and uncurved model membrane vesicles: "Nature's own" fusogenic lipid bilayer. *Biochemistry* **2001**, *40*, 4340−4348.
(75) Haque, M. E.; Lentz, B. R. Roles of curvature and hydrophobic interstice energy in fusion: Studies of lipid perturbant effects. *Biochemistry* **2004**, *43*, 3507−3517.
(76) Epand, R. M.; Epand, R. F.; Ahmed, N.; Chen, R. Promotion of hexagonal phase formation and lipid mixing by fatty acids with varying degrees of unsaturation. *Chem. Phys. Lipids* **1991**, *57*, 75−80.
(77) Treen, M.; Uauay, R. D.; Jameson, D. M.; Thomas, V. L.; Hoffman, R. R. Effect of docosahexaenoic acid on membrane fluidity and function in intact cultured Y-79 retinoblastoma cells. *Arch. Biochem. Biophys.* **1992**, *294*, 564−570.
(78) Stulnig, T. M.; Huber, J.; Leitinger, N.; Imre, E. M.; Angelisova, P.; Nowotny, P.; Waldhausl, W. Polyunsaturated eicosapentaenoic acid displaces proteins from membrane rafts by altering raft lipid composition. *J. Biol. Chem.* **2001**, *276*, 37335−37340.
(79) Shaikh, S. R.; Brown, D. A. Models of plasma membrane organization can be applied to mitochondrial membranes to target human health and disease with polyunsaturated fatty acids. *Prostaglandins, Leukotrienes Essent. Fatty Acids* **2013**, *88*, 21−25.
(80) Shaikh, S. R.; Jolly, C. A.; Chapkin, R. S. n-3 Polyunsaturated fatty acids exert immunomodulatory effects on lymphocytes by targeting plasma membrane molecular organization. *Mol. Aspects Med.* **2012**, *33*, 46−54.
(81) Corsetto, P. A.; Cremona, A.; Montorfano, G.; Jovenitti, I. E.; Orsini, F.; Arosio, P.; Rizzo, A. M. Chemical-physical changes in cell membrane microdomains of breast cancer cells after omega-3 PUFA incorporation. *Cell Biochem. Biophys.* **2012**, *64*, 45−59.
(82) Bousquet, M.; Calon, F.; Cicchetti, F. Impact of omega-3 fatty acids in Parkinson's disease. *Ageing Res. Rev.* **2011**, *10*, 453−463.
(83) Calon, F.; Cole, G. Neuroprotective action of omega-3 polyunsaturated fatty acids against neurodegenerative diseases: evidence from animal studies. *Prostaglandins, Leukotrienes Essent. Fatty Acids* **2007**, *77*, 287−293.
(84) Bourre, J. M. Roles of unsaturated fatty acids (especially omega-3 fatty acids) in the brain at various ages and during ageing. *J. Nutr., Health Aging* **2004**, *8*, 163−174.
(85) Collie-Duguid, E. S. R.; Wahle, K. W. J. Inhibitory effect of fish oil n-3 polyunsaturated fatty acids on the expression of endothelial cell adhesion molecules. *Biochem. Biophys. Res. Commun.* **1996**, *220*, 969−974.
(86) Bates, E. J.; Ferrante, A.; Harvey, D. P.; Poulos, A. Polyunsaturated fatty acids increase neutrophil adherence and integrin receptor expression. *J. Leukocyte Biol.* **1993**, *53*, 420−426.
(87) Florent, S.; Malaplate-Armand, C.; Youssef, I.; Kriem, B.; Koziel, V.; Escanyé, M.-C.; Fifre, A.; Sponne, I.; Leininger-Muller, B.; Olivier, J.-L.; Pillot, T.; Oster, T. Docosahexaenoic acid prevents neuronal apoptosis induced by soluble amyloid-beta oligomers. *J. Neurochem.* **2006**, *96*, 385−395.
(88) Wang, J.; Song, M. Y.; Bae, U. J.; Lim, J. M.; Kwon, K. S.; Park, B. H. n-3 Polyunsaturated fatty acids protect against pancreatic β-cell damage due to ER stress and prevent diabetes development. *Mol. Nutr. Food Res.* **2015**, *59*, 1791−1802.
(89) Sekikawa, A.; Doyle, M. F.; Kuller, L. H. Recent findings of long-chain n-3 polyunsaturated fatty acids (LCn-3 PUFAs) on atherosclerosis and coronary heart disease (CHD) contrasting studies in Western countries to Japan. *Trends Cardiovasc. Med.* **2015**, *25*, 717−723.
(90) Ganança, L.; Galfalvy, H. C.; Oquendo, M. A.; Hezghia, A.; Cooper, T. B.; Mann, J. J.; Sublette, M. E. Lipid correlates of antidepressant response to omega-3 polyunsaturated fatty acid supplementation: A pilot study. *Prostaglandins, Leukotrienes Essent. Fatty Acids* **2017**, *119*, 38−44.
(91) Czysz, A. H.; Rasenick, M. M. G-protein signaling, lipid rafts and the possible sites of action for the antidepressant effects of n-3 polyunsaturated fatty acids. *CNS Neurol. Disord.: Drug Targets* **2013**, *12*, 466−473.
(92) Kristensen, S.; Schmidt, E. B.; Schlemmer, A.; Rasmussen, C.; Johansen, M. B.; Christensen, J. H. Beneficial effect of n-3 polyunsaturated fatty acids on inflammation and analgesic use in psoriatic arthritis: a randomized, double blind, placebo-controlled trial. *Scand. J. Rheumatol.* **2018**, *47*, 27−36.
(93) Yaqoob, P. Mechanisms underlying the immunomodulatory effects of n-3 PUFA. *Proc. Nutr. Soc.* **2010**, *69*, 311−315.
(94) Georgiou, T.; Wen, Y. T.; Chang, C. H.; Kolovos, P.; Kalogerou, M.; Prokopiou, E.; Neokleous, A.; Huang, C. T.; Tsai, R. K. Neuroprotective Effects of omega-3 polyunsaturated fatty acids in a rat model of anterior ischemic optic neuropathy. *Invest. Ophthalmol. Visual Sci.* **2017**, *58*, 1603−1611.
(95) Fritsche, K. L.; Byrge, M.; Feng, C. Dietary omega-3 polyunsaturated fatty acids from fish oil reduce interleukin-12 and interferon-gamma production in mice. *Immunol. Lett.* **1999**, *65*, 167−173.

DOI: 10.1021/acsomega.7b01935
ACS Omega 2018, 3, 3235−3247

(96) Gorjão, R.; Azevedo-Martins, A. K.; Rodrigues, H. G.; Abdulkader, F.; Arcisio-Miranda, M.; Procopio, J.; Curi, R. Comparative effects of DHA and EPA on cell function. *Pharmacol. Ther.* **2009**, *122*, 56−64.
(97) Carpentier, Y. A.; Hacquebard, M. Intravenous lipid emulsions to deliver omega 3 fatty acids. *Prostaglandins, Leukotrienes Essent. Fatty Acids* **2006**, *75*, 145−148.
(98) Shinde, R. L.; Devarajan, P. V. Docosahexaenoic acid-mediated, targeted and sustained brain delivery of curcumin microemulsion. *Drug Delivery* **2017**, *24*, 152−161.
(99) Guerzoni, L. P. B.; Nicolas, V.; Angelova, A. *In vitro* modulation of TrkB receptor signaling upon sequential delivery of curcumin-DHA loaded carriers towards promoting neuronal survival. *Pharm. Res.* **2017**, *34*, 492−505.
(100) Lidich, N.; Aserin, A.; Garti, N. Structural characteristics of oil-poor dilutable fish oil omega-3 microemulsions for ophthalmic applications. *J. Colloid Interface Sci.* **2016**, *463*, 83−92.
(101) Desai, A.; Vyas, T.; Amiji, M. Cytotoxicity and apoptosis enhancement in brain tumor cells upon coadministration of paclitaxel and ceramide in nanoemulsion formulations. *J. Pharm. Sci.* **2008**, *97*, 2745−2756.
(102) Angelova, A.; Garamus, V. M.; Angelov, B.; Tian, Z.; Li, Y.; Zou, A. Advances in structural design of lipid-based nanoparticle carriers for delivery of macromolecular drugs, phytochemicals and anti-tumor agents. *Adv. Colloid Interface Sci.* **2017**, *249*, 331−345.
(103) Zerkoune, L.; Lesieur, S.; Putaux, J.-L.; Choisnard, L.; Gèze, A.; Wouessidjewe, D.; Angelov, B.; Vebert-Nardin, C.; Doutch, J.; Angelova, A. Mesoporous self-assembled nanoparticles of biotransesterified cyclodextrins and nonlamellar lipids as carriers of water-insoluble substances. *Soft Matter* **2016**, *12*, 7539−7550.
(104) Hamilton, J. A.; Cistola, D. P. Transfer of oleic acid between albumin and phospholipid vesicles. *Proc. Natl. Acad. Sci. U.S.A.* **1986**, *83*, 82−86.
(105) Cistola, D. P.; Hamilton, J. A.; Small, D. M.; Jackson, D. The ionization and phase behavior of fatty acids in water: Application of the Gibbs phase rule. *Biochemistry* **1988**, *27*, 1881−1888.
(106) Börjesson, S. I.; Hammarström, S.; Elinder, F. Lipoelectric modification of ion channel voltage gating by polyunsaturated fatty acids. *Biophys. J.* **2008**, *95*, 2242−2253.
(107) Petrov, I.; Angelova, A. Interaction free energies in Langmuir-Blodgett multilayers of docosylammonium phosphate. *Langmuir* **1992**, *8*, 3109−3115.
(108) Blanchet, C. E.; Spilotros, A.; Schwemmer, F.; Graewert, M. A.; Kikhney, A. G.; Jeffries, C. M.; Franke, D.; Mark, D.; Zengerle, R.; Cipriani, F.; Fiedler, S.; Roessle, M.; Svergun, D. I. Versatile sample environments and automation for biological solution X-ray scattering experiments at the P12 beamline (PETRA III, DESY). *J. Appl. Crystallogr.* **2015**, *48*, 431−443.

DOI: 10.1021/acsomega.7b01935
ACS Omega 2018, 3, 3235−3247